Modeling and Reduction of Radiated EMI in Non-isolated Power Converters in Automotive Applications

Juntao Yao and Shuo Wang
Department of Electrical and Computer Engineering
University of Florida, Gainesville, FL, USA

Zheng Luo
Monolithic Power Systems, Inc.
San Jose, CA, USA

***Abstract*—This paper develops modeling and reduction techniques of the radiated electromagnetic interference (EMI) in non-isolated power converters in automotive applications. In modeling investigations, noise source models and the antenna models are developed to reveal the generation of the common mode (CM) noise and the radiated EMI in the investigated buck-boost power converter. The developed models can predict the radiated EMI with clear physical meanings of the switching noise, the power converter topology, and the PCB parasitics. The influences of the PCB ground layer parasitics on the radiated EMI are first revealed. In noise reduction investigations, several techniques are proposed including 1) PCB layout improvement for reducing the parasitics of the ground layer and 2) circuit topology improvement including the addition of a capacitor across the input and output nodes and improvement of the PCB traces connecting the cross capacitor. Experimental verifications of the radiated modeling and reduction techniques are conducted on a buck-boost power converter in automotive lighting applications.**

***Index Terms*—Radiated emission, electromagnetic interference (EMI), radiated EMI, common mode, non-isolated power converter**

I. Introduction

The radiated EMI in power electronics systems in automotive applications is regulated by many international standards, such as CISPR25 [1-3]. It is essential to develop modeling and noise reduction techniques for the radiated EMI in power converters in automotive applications [1, 4].

To predict the radiated EMI caused by the CM current, some researches focus on the CM current measurement technique and the CM current information based radiated EMI prediction [4]. The spatial distribution of the CM current, including the magnitude and phase information, can be extracted by measurements. Based on the extracted spatial distribution of the CM current, a multi-dipole model is built for predicting the radiated EMI [4]. Specifically, the cable bundle is divided into short segments and modeled as a set of distributed Hertzian dipoles. The radiated EMI is calculated as the superposition of the resulted electromagnetic fields of the distributed Hertzian dipoles [4, 5]. The existing researches can develop a transfer function to characterize the relationship between the CM current and the radiated EMI. However, the CM current is a middle parameter between the noise sources generated by the power converter and the radiated EMI generated by the power cables attached to the power converter. It is essential to characterize the CM noise generation mechanism in the power converter system.

To describe the CM behavior of the power converter, some researches have developed an equivalent CM behavioral model of the power converter. The equivalent CM behavioral model is reconstructed by the terminal parameters including the CM current and the CM terminal impedances [6]. The equivalent CM noise sources and impedances are reconstructed for representing the equivalent CM behavioral model of the power converter. However, the terminal behavioral model does not have a clear relation with the physical parameters of the power converter. Such a black-box model needs to be improved. And it is essential to develop models with physical meanings of the power converter parameters.

With the consideration of physical meanings of the power converter parameters, extensive existing researches have revealed the fundamental mechanisms of the noise generation in isolated power converters in consumer electronics applications like power adapters [7-9]. In isolated power converters, CM noise is usually transformed from the switching noises through the isolation transformer's interwinding parasitics [9, 10]. The CM noise generation mechanism in non-isolated power converters has significant differences from that in isolated power converters. While in non-isolated power converters, there is no isolation transformer and the CM noise generation mechanism is different [11].

In some non-isolated power converters, the pulsating voltages and the parasitic couplings can act as the radiation excitation sources [12]. In [12], the equivalent source voltage and the stray capacitance are investigated using the transverse electromagnetic (TEM) cell. In the full-wave simulation, the radiated EMI from the cable antenna is simulated [12]. However, the relationship between the converter and the radiated EMI is not disclosed [13]. And when the converter topology and the testing setup are complicated, the extraction of the equivalent source is not simple or straightforward [13]. Moreover, this model assumes the parasitic capacitance between pulsating nodes and the ground plays a big role in a monopole antenna which includes one attached cable. But this mechanism does not apply to this paper's study case with the input/output cables as the radiation antenna and with the voltage

This research was supported by Monolithic Power Systems, Inc.

difference between input and output nodes as the radiation excitation.

Further investigations are needed to develop models with clear physical meanings to reveal the mechanisms of the noise generation and transformation in non-isolated power converters. And critical parameters need to be identified and improved for noise reductions.

This paper will develop modeling and reduction techniques of radiated EMI in non-isolated power converters in automotive applications, and specifically has several objectives. 1) Develop the models for the noise circuit of the power converter, a) with clear physical meanings of the noise sources, parasitic impedances, b) with the considerations of physical components and PCB; 2) Develop the models for the radiation antenna; 3) Base on the developed models, develop guidelines for reducing the radiated EMI.

This paper is organized as follows. In the second section, this paper will present the modeling of the noise circuit and the antenna. In the third section, noise reduction techniques including the circuit topology improvement and the PCB improvement will be proposed and verified. In each section, simulation and experimental verifications are included.

II. Development of Radiated EMI Noise Models in Non-isolated Power Converters

A. Noise source model

Fig. 1 shows a buck-boost converter in automotive lighting applications. The system includes the battery, the power converter (as the LED driver), the LED headlights (as the load) and the attached input and output power cables. In Fig. 1, according to the regulation standard CISPR 25, the length of the input cable between the battery and the LED driver power converter is 1.5m and according to the practical application setup, the length of the output cable between the LED driver power converter and the LED light is 0.5m. The input and output power cables form the antenna. And the antenna is driven by the voltage difference V_{P3P1} between the input node P_1 and the output node P_3 of the buck-boost power converter, which is called as the CM terminal voltage. The resulted CM current flows through the attached power cables causing the radiated EMI.

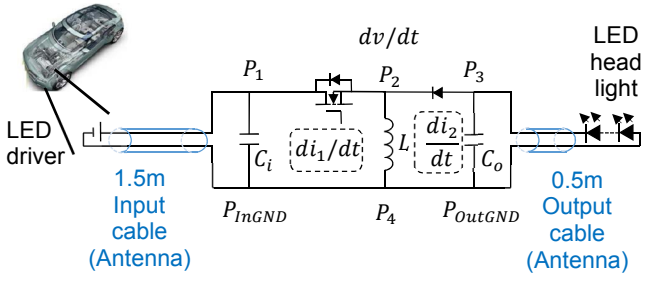

Fig. 1. Non-isolated power converters applied as automotive LED drivers

About the CM noise generation mechanisms in the non-isolated power converter, if the ground layer is ideal and has zero parasitics and zero impedance. The voltage drop on the ideal ground layer would be zero. Further with the small impedance of the decoupling capacitors neglected, the voltage difference V_{P3P1} would be zero. If under this ideal condition, the radiation excitation for the antenna consisting of the input and output power cables would be zero. And the resulted radiated EMI from the power cables would be zero.

However, in reality, there are parasitic impedances of the physical PCB traces. Though those parasitics are not shown in the schematics, their impacts on the noise generation and the radiated EMI are significant. Fig. 2 shows the parasitic impedances of the ground layer, which has the impedance magnitude reaching the 10^0 and 10^1 orders at high frequencies. Voltage drops can be induced on the parasitic impedances of the ground layer. In the investigated buck-boost converter, V_{P3P1} is due to the voltage drops on the parasitic impedances of the nonideal ground layer. With the consideration of the operating principle of the buck-boost converter, the ground layer is divided into several segments according to the operating intervals and the sub-circuits. Specifically, the ground layer is divided into two segments, respectively the segment between P_{InGND} and P_4, and the segment between P_4 and P_{OutGND}. Note that, in Fig. 2, the decoupling capacitors' impedances are negligible as compared with those of the ground layers. As a result, the differential mode voltage drops on the decoupling capacitors are very small and are neglected in the radiated EMI analyses. The CM terminal voltage between P_1 and P_3 approximately equals to the voltage difference between P_{InGND} and P_{OutGND}.

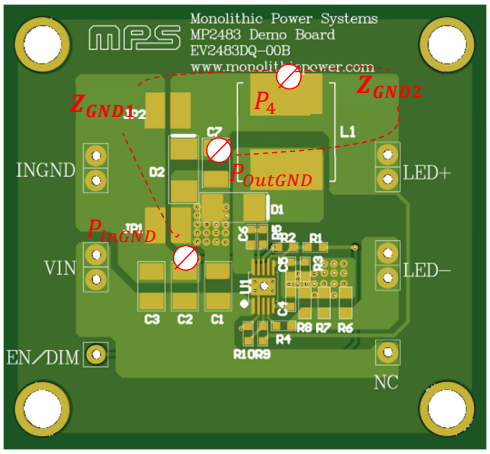

(a)

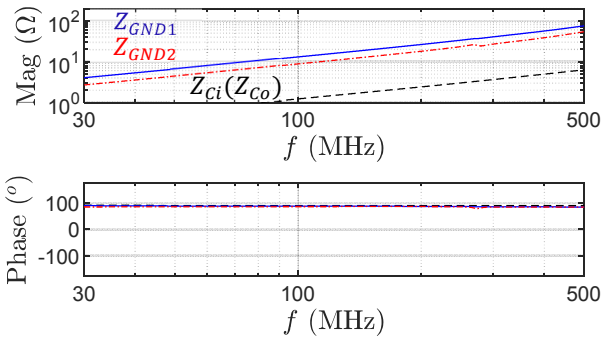

(b)

Fig. 2. Parasitic impedances of the ground layer (a) ground layer nodes on the physical power converter (b) extracted impedances

To analyze the noise circuit consisting of the switching devices and the parasitic impedances of the ground layer as shown in Fig. 3 (a), switching devices are replaced by voltage/current sources according to the substitution theorem, as shown in Fig. 3 (b).

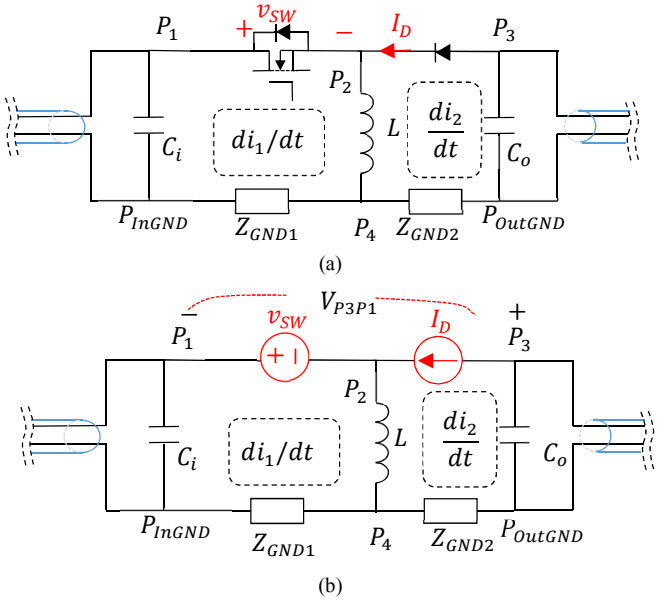

Fig. 3. Noise circuit of the buck-boost power converter (a) The converter circuit with the parasitic impedances of the ground layer (b) Switching devices replaced by voltage/current sources

The noise transformation from the two noise sources to the CM terminal voltage V_{P3P1} can be analyzed based on the noise circuit using the superposition theorem.

The contribution from V_{SW} to the CM terminal voltage is

$$V_{P3P1\_VSW} = -V_{SW} \cdot \frac{Z_{GND1}}{Z_{GND1}+Z_L} \quad (1)$$

where a transfer function is extracted to characterize the transformation from V_{SW} to the CM terminal voltage as

$$G_{VP3P1\_VSW} = \frac{V_{P3P1\_VSW}}{V_{SW}} = -\frac{Z_{GND1}}{Z_{GND1}+Z_L} \quad (2)$$

The contribution from I_D to the CM terminal voltage is

$$V_{P3P1\_ID} = -I_D \cdot ((Z_{GND1}||Z_L) + Z_{GND2}) \quad (3)$$

where a transfer function is also extracted to characterize the transformation from I_D to the CM terminal voltage, as

$$G_{VP3P1\_ID} = \frac{V_{P3P1\_ID}}{I_D} = -((Z_{GND1}||Z_L) + Z_{GND2}) \quad (4)$$

According to the superposition theorem, the total V_{P3P1} equal to

$$V_{P3P1} = V_{P3P1\_VSW} + V_{P3P1\_ID} \quad (5)$$

With (1) and (3) substituted to (2.c1), the total V_{P3P1} is calculated as

$$V_{P3P1} = -V_{SW} \cdot \frac{Z_{GND1}}{Z_{GND1}+Z_L} - I_D \cdot ((Z_{GND1}||Z_L) + Z_{GND2}) \quad (6)$$

To simplify the expression, with (2) and (4) substituted to (5), the total V_{P3P1} is expressed as

$$V_{P3P1} = V_{SW} \cdot G_{VP3P1\_VSW} + I_D \cdot G_{VP3P1\_ID} \quad (7)$$

As the switching noises, V_{SW} and I_D are measured. The time-domain waveform and the spectrums are shown in Fig. 4. Note that, the bandwidth of the voltage probe (Rigol RP3500A) is 500MHz. And from the measured waveforms and the spectrums, except for the spectrum bumps due to the ringing around 140 MHz, the noise spectrums of V_{SW} and I_D decreases at high frequencies.

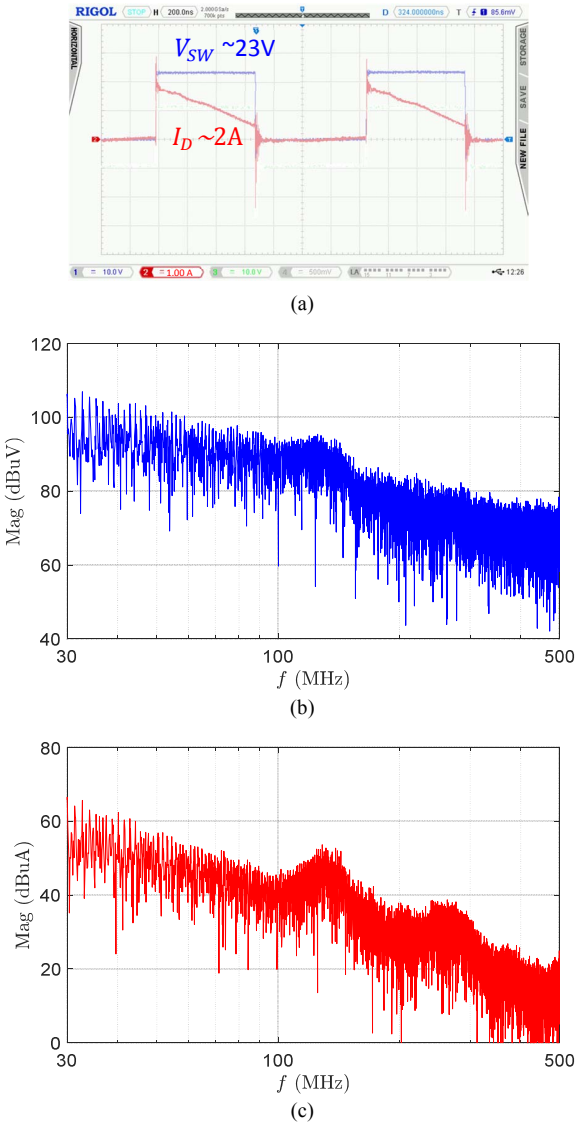

Fig. 4. Waveforms and spectrums of the noise sources (a) waveforms (b) V_{SW} spectrum (c) I_D spectrum

The transfer gains of G_{VP3P1_VSW} and G_{VP3P1_ID} are extracted, as shown in Fig. 5.

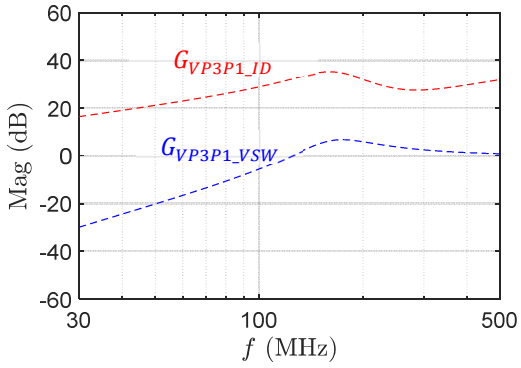

Fig. 5. Noise transfer gains of G_{VP3P1_VSW} and G_{VP3P1_ID}

With the switching noises measured and the noise transfer

gains extracted, according to (7), V_{P3P1} can be predicted, as shown in Fig. 6. The predicted V_{P3P1} can match the measured. And the noise source model is verified.

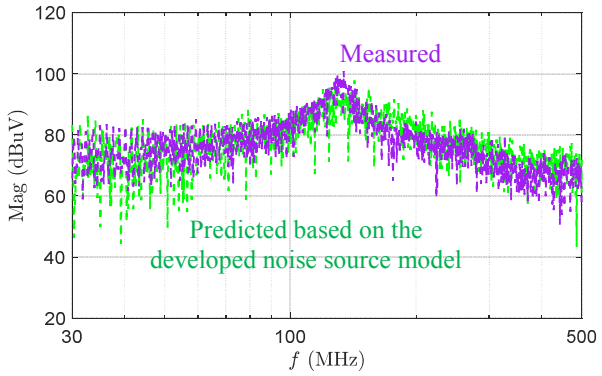

Fig. 6. Comparison of the measured and predicted CM terminal voltage spectrums

B. Antenna model

Fig. 7 shows the diagram of the power cable arrangement according to CISPR 25. Fig. 8 shows the Thevenin equivalence of the cable antenna and the radiation excitation, where R_L is the loss resistance along antenna arms, R_r is the radiation resistance, X_A is the reactance of antenna to represent the near field energy, and $Z_{Antenna} = R_L + R_r + jX_A$ is antenna impedance at terminals, Z_{CMConv} is the source impedance of the power converter.

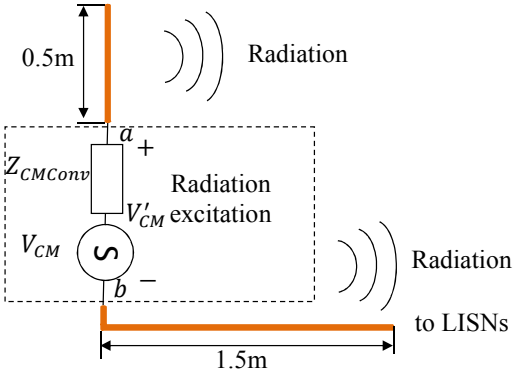

Fig. 7. Cable antenna and the equivalent radiation excitation source

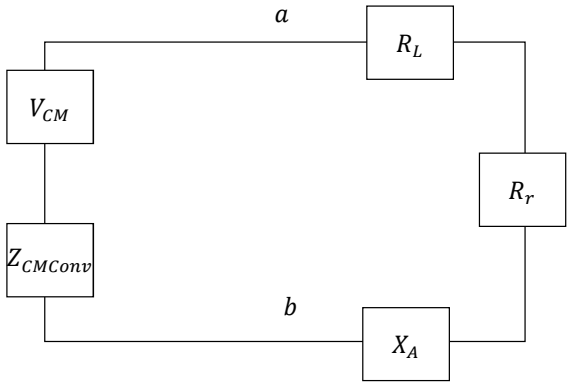

Fig. 8. Thevenin equivalence of the antenna and the excitation

The power delivered to the cable antenna for radiation is

$$P_r = \frac{1}{2}|I_{CM}|^2 R_r = \frac{|V_{CM}|^2}{2}\left[\frac{R_r}{|Z_{CMConv}+R_L+R_r+jX_A|^2}\right] \quad (8)$$

In the far field region, in the equivalent isotropic and uniform radiation case, the relation between the radiated power and the radiated electric field intensity E is

$$P_r = \frac{E^2}{2\eta}\cdot 4\pi r^2 \quad (9)$$

which can be expressed as

$$E = \sqrt{P_r \eta / 2\pi r^2} \quad (10)$$

where r is the distance between the radiation antenna and the observation point, η is the characteristic impedance $120\pi\ \Omega$.

With (8) substituted to (10), derives

$$E = |V_{CM}| \cdot \sqrt{\frac{1}{4}\left[\frac{R_r}{|Z_{CMConv}+R_L+R_r+jX_A|^2}\right]\cdot\frac{\eta}{\pi r^2}} \quad (11)$$

which indicates that the radiated electric field intensity E is proportional to the magnitude $|V_{CM}|$ by a transfer gain. And the transfer gain of the antenna is designated as

$$G_{VCM} = \sqrt{\frac{1}{4}\left[\frac{R_r}{|Z_{CMConv}+R_L+R_r+jX_A|^2}\right]\cdot\frac{\eta}{\pi r^2}} \quad (12)$$

In the CISPR 25 setup, for the case without the CM choke, the converter's CM impedance Z_{CMConv} is small and negligible as compared with antenna's impedance $Z_{Antenna} = R_L + R_r + jX_A$. (13) can be reduced as

$$G'_{VCM} = \sqrt{\frac{1}{4}\left[\frac{R_r}{|R_L+R_r+jX_A|^2}\right]\cdot\frac{\eta}{\pi r^2}} \quad (13)$$

G'_{VCM} can be extracted by experiments. In the experiments, an excitation voltage $|V'_{CM}|$ is added to the terminals of the power cables. A gain between the excitation voltage $|V'_{CM}|$ and the resulted radiated electric field intensity E' can be extracted as

$$G'_{VCM} = \frac{E'}{|V'_{CM}|} \quad (14)$$

The extracted gain of G'_{VCM} is shown in Fig. 9. The G'_{VCM} has the bumps around 100 MHz, 150 MHz, 200 MHz, 250 MHz, 300 MHz, and 400 MHz, which are the intrinsic characteristics of the power cable antenna in the CISPR25 testing setup.

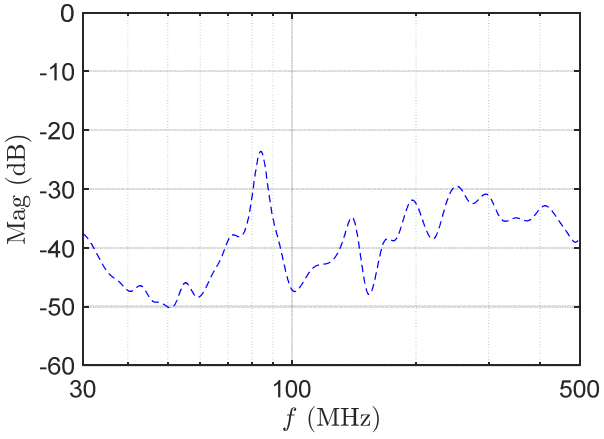

Fig. 9. Antenna's transfer gain between excitation voltage and the resulted radiated EMI intensity

C. Radiated EMI prediction

With the CM terminal voltage and the antenna's transfer gain predicted, the radiated EMI can be predicted based on the flowchart shown in Fig. 10. The comparison of the predicted

and the measured radiated EMI is shown in Fig. 11.

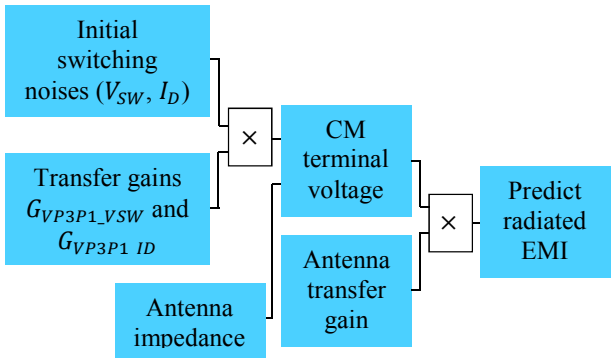

Fig. 10. Radiated EMI prediction procedure

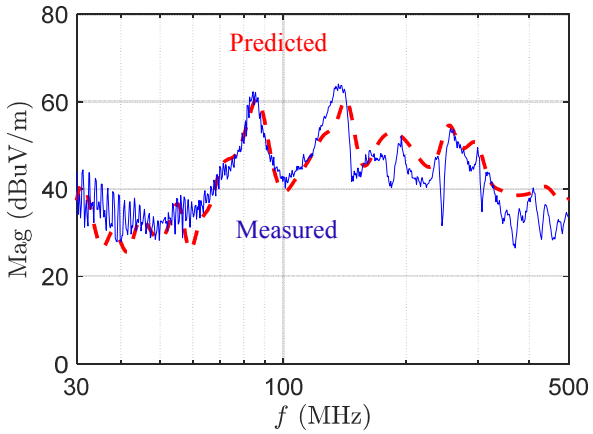

Fig. 11. Comparison of measured and predicted radiated EMI

From Fig. 11, the radiated EMI predicted based on the CM terminal voltage and the cable antenna's transfer gain, can match the measured. The antenna model and the radiated EMI prediction are verified.

To summarize the EMI noise model researches, 1) in the noise source model, the switching voltages and currents in the converter can transform to be the CM terminal voltages due to the parasitic impedance of the ground layer, and the impedances of ground layer are important 2) in the antenna model of the power cables, the power converter's CM terminal voltage is the radiation excitation driving the cable antenna radiating to space, and the cable antenna is a critical factor causing part of the radiated EMI bumps.

Based on the modeling researches, the radiated EMI can be reduced by reducing CM terminal voltage and by reducing the antenna's transfer gain. While the transfer gain of the cable antenna is an intrinsic parameter of the arranged power cables determined by the CISPR 25 standard and by the application scenario and cannot be changed. To reduce the radiated EMI, the feasible approach is by reducing radiation excitation noise generated by the power converter.

III. Noise Reduction Techniques of Circuit Topology Improvement and PCB Layout Improvement

In the study case of the buck-boost power converter with power cables attached, since the CM terminal voltage is the radiation excitation noise, it is essentially important to develop noise reduction techniques by reducing the CM terminal voltage.

The CM terminal voltage is the result of the superimposed voltage drops on the ground layer. In order to reduce the CM terminal voltage, reducing the ground layer impedance will be helpful. Based on the analyses, there are two approaches: 1) by improving the ground layer layout, the improved ground layer layout can reduce the parasitic impedances and the voltage drops; 2) by the improvement of the circuit topology, an addition of cross capacitors with small impedances at high frequencies connected in parallel with the ground layer can equivalently reduce parasitic impedances and can reduce the voltage drops on the ground layer.

A. PCB parasitics analysis and improvement for noise reduction

The parasitic impedance of the ground layer/trace is predominantly equivalent series inductance (ESL) at high frequencies. The ESL of the flat wire can be calculated as

$$L_{flat} = 2\cdot\ell\left[\ln\left(\frac{2\cdot\ell}{w+t}\right)+0.5+0.2235\cdot\frac{w+t}{\ell}\right]$$
$$= 2\cdot\ell\cdot\ln\left(\frac{2\cdot\ell}{w+t}\right)+\ell+0.447\cdot(w+t)\ \text{[nH]} \quad (15)$$

Where ℓ is the length in cm, w is the width in cm, t is the thickness in cm

$$\frac{\partial L_{flat}}{\partial \ell} = 2\cdot(w+t)+1 \quad (16)$$

$$\frac{\partial L_{flat}}{\partial t} = -(w+t)\cdot 2\cdot\ell\cdot\frac{1}{(w+t)^2}+0.447$$
$$= -2\cdot\ell\cdot\frac{1}{w+t}+0.447 \quad (17)$$

The thickness t is in the order of 10^{-3} cm,

$$\left|\frac{\partial L_{flat}}{\partial t}\Delta t\right| < \left|\frac{\partial L_{flat}}{\partial \ell}\Delta\ell\right| \quad (18)$$

in practical dimension parameters, with ℓ ~10^0 cm, w ~10^0 cm and t ~10^{-3} cm. Given the practical dimension parameters, L_{flat} is more sensitive to the trace length than to the thickness.

In the investigation case study, given the ground layer length, thick plates of 1.0 cm soldering tin are applied in parallel with the ground layer (original thickness 0.0035 cm), as shown in Fig. 12. The application of thick ground layer will have limited effect for reducing the ESL. For example, given the trace width 1 cm, length 4cm, with the thickness increased from 0.0035 cm to 1 cm, the inductance is reduced from 21.06 nH to 15.98 nH, reduced to 75.6% (-2.4 dB). As a result, regarding the radiated EMI, although it can be reduced, as shown in Fig. 13, the reduction is limited around -3 dB.

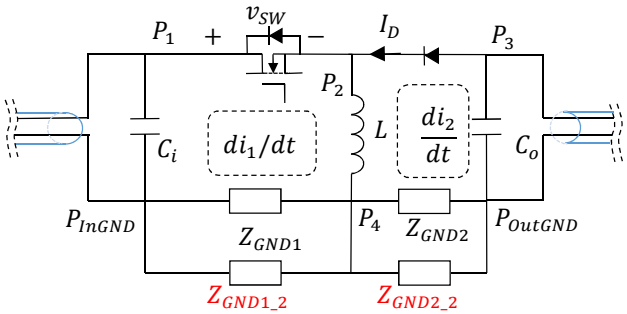

Fig. 12. Application of the thick ground trace

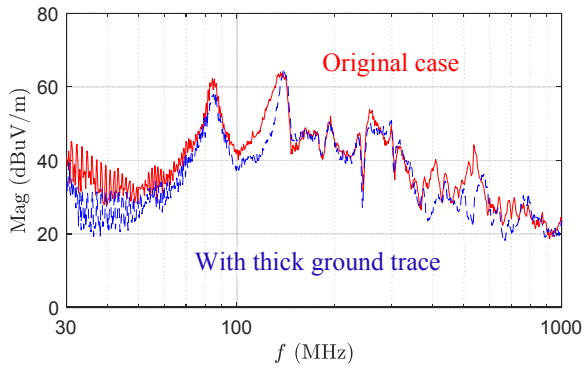

Fig. 13. Radiated EMI before and after the application of thick ground trace

B. *Circuit topology improvement and noise circuit analyses*

A capacitor can be applied across the input and output nodes, which is connected (or equivalently connected) in parallel with the ground layer, as shown in Fig. 14. It should be pointed out because the distance between P_1 and P_3 on the PCB is much smaller than that between P_{InGND} and P_{OutGND}, the cross capacitor is applied between P_1 and P_3 for reducing the trace length and the induced ESL.

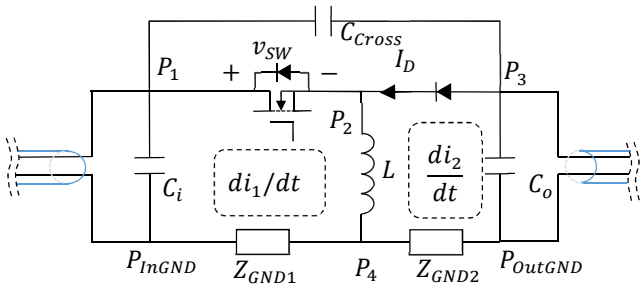

Fig. 14. Buck-boost converter with the cross capacitor applied

After the application of the cross capacitor, the contribution from V_{SW} to V_{P3P1} is

$$V_{P3P1\_VSW} = -V_{SW} \cdot \frac{Z_{GND1}||(Z_{GND2}+Z_{Ccross})}{Z_{GND1}||(Z_{GND2}+Z_{Ccross})+Z_L} \quad (19)$$

and the transfer function to characterize the transformation from V_{SW} to the CM terminal voltage is

$$G_{VP3P1\_VSW} = \frac{V_{P3P1\_VSW}}{V_{SW}} = -\frac{Z_{GND1}||(Z_{GND2}+Z_{Ccross})}{Z_{GND1}||(Z_{GND2}+Z_{Ccross})+Z_L} \quad (20)$$

The contribution from I_D to the CM terminal voltage is

$$V_{P3P1\_ID} = -I_D \cdot (((Z_{GND1}||Z_L)+Z_{GND2})||Z_{Ccross}) \quad (21)$$

and the transfer function to characterize the transformation from I_D to the CM terminal voltage is

$$G_{VP3P1\_ID} = \frac{V_{P3P1\_VSW}}{I_D} = -(((Z_{GND1}||Z_L)+Z_{GND2})||Z_{Ccross}) \quad (22)$$

The noise transfer gains before and after the application of the cross capacitor (for example, a ceramic capacitor, 1uF) are compared in Fig. 15. The application of cross capacitor is effective to reduce the transfer gains.

After the application of the cross capacitor, the switching noise is compared with the original case. The time-domain waveforms are shown in Fig. 16. The cross capacitor has a negligible influence on the slew rates of the switching noise, but it can influence the ringing frequency and magnitude.

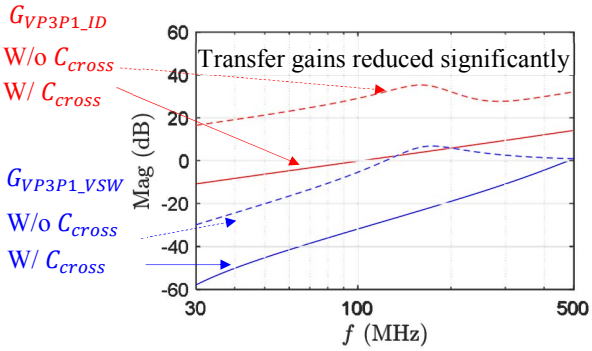

Fig. 15. Comparison of noise transfer gains

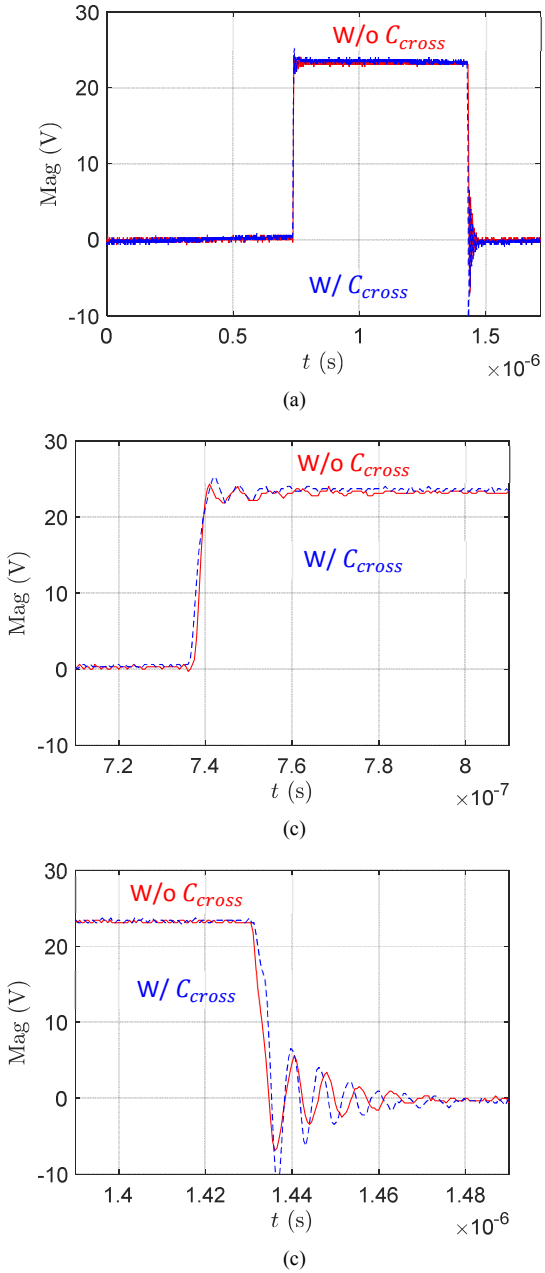

Fig. 16. Comparison of V_{SW} before and after the application of the cross capacitor (a) whole waveform (b) switching-off transition (c) switching-on transition

The spectrums of the switching noise before and after the application of the cross capacitor are compared, as shown in Fig. 17. Since at most frequencies (especially <100MHz), the spectrum is determined by the slew rates which are almost unchanged after the application of the cross capacitor, the spectrum is almost unchanged at most frequencies. The application of the cross capacitor can influence the ringing frequency and magnitude but it does not reduce the switching noise spectrum overall. For the switching noise I_D , the application of the cross capacitor also does not influence most frequencies and merely influences the ringing and the corresponding spectrum. In summary, the application of the cross capacitor does not have a significant influence on the switching noises, although it can equivalently reduce the ground layer's impedance and the noise transfer gain significantly.

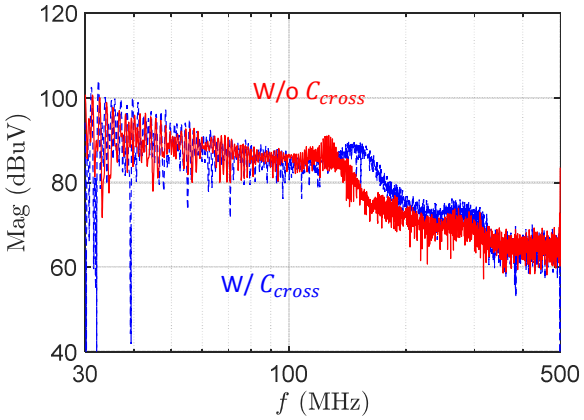

Fig. 17. Comparison of V_{SW} spectrums before and after the application of the cross capacitor

The application of the cross capacitor can effectively reduce the noise transfer gains, and the CM terminal voltage is reduced effectively, as shown in Fig. 18. Both the time domain waveform and the spectrums can show significant reductions.

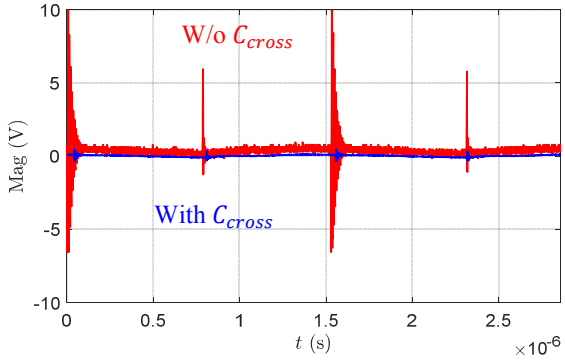

(a)

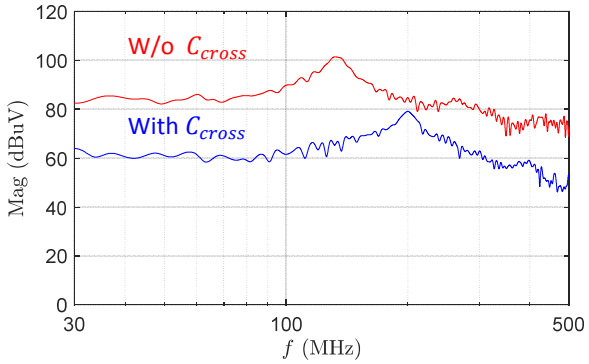

(b)

Fig. 18. Comparison of V_{P3P1} before and after the application of the cross capacitor (a) time-domain waveforms (b) spectrums

With the CM terminal voltage reduced by the application of the cross capacitor, the radiated EMI is reduced accordingly, as shown in Fig. 19.

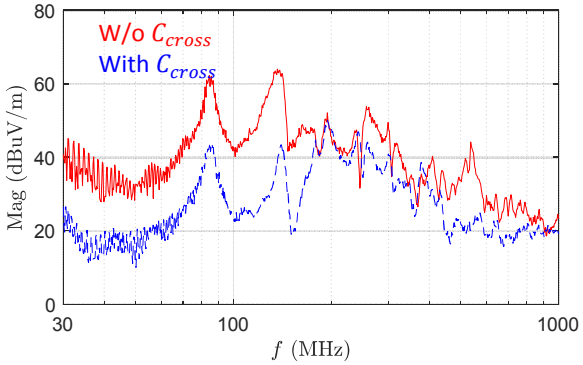

Fig. 19. Radiated EMI before and after the application of the cross capacitor

After the application of the cross capacitor, the parasitics impedances of the traces connecting the cross capacitor is in series connection with the cross capacitor, as shown in Fig. 20. Except for the parasitic impedance of the ground layer/trace, there is another type of layer/trace influential for the radiated EMI. The parasitic impedances of the traces can be larger than the cross capacitor's impedance at high frequencies. As a result, the effect of the cross capacitor for reducing the radiated EMI is degraded.

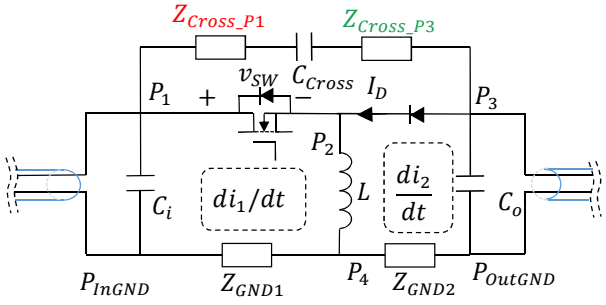

(a)

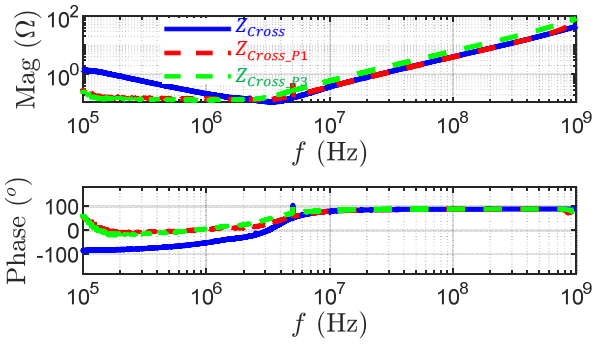

(b)

Fig. 20. Parasitics impedances of the traces connecting the cross capacitor (a) Circuit with the cross capacitor and the parasitic impedances (b) Extracted impedances

To further improve the noise reduction effect of the cross capacitor, it is essentially important to improve the layout to minimize the parasitics of the traces connecting the cross capacitor. As a case study, thick plates of 1 cm soldering tin are connected in parallel with the traces connecting the cross capacitor as shown in Fig. 21. The radiated EMI can be further reduced (around -3 dB) as compared with the case with the application of the cross capacitor, as shown in Fig. 22.

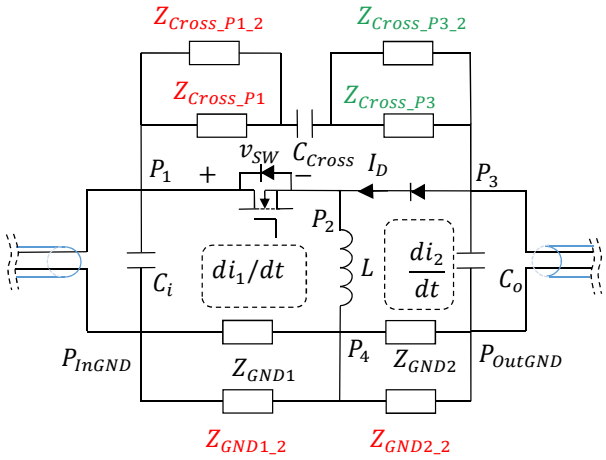

Fig. 21. Investigation of the thick trace applied to the traces connecting the cross capacitor (W/ C_{Cross})

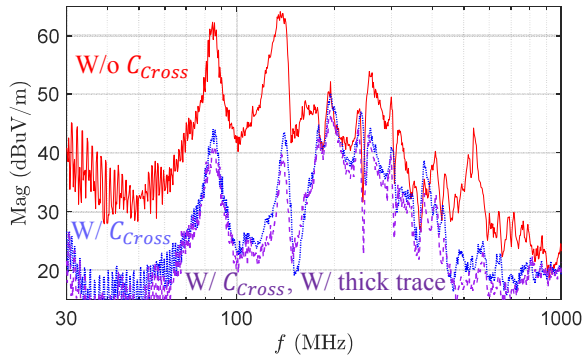

Fig. 22. Radiated EMI before and after the application of thick traces applied (W/ C_{Cross})

In summary of the noise reduction techniques, it is effective to reduce the radiated by 1) the improved PCB layout by reducing the trace length and increasing the trace thickness 2) the application of cross capacitor and the improvement of connection traces.

IV. CONCLUSIONS

Modeling and noise reduction techniques of radiated EMI in non-isolated power converters in automotive applications are verified. Based on the developed noise source model and the antenna model, the radiated EMI can be predicted. And based on the modeling, influence parameters like the ground layer impedances are identified. To reduce the radiated EMI in non-isolated power converters in automotive applications, preliminary guidelines are developed, including 1) the application of the cross capacitor with small ESL and 2) the improvement of the PCB layout by reducing the trace length and increasing the trace thickness or the layer quantity.

REFERENCES

[1] C. Nan, R. Ayyanar, and Y. Xi, "A 2.2-MHz Active-Clamp Buck Converter for Automotive Applications," *IEEE Transactions on Power Electronics,* vol. 33, pp. 460-472, 2018.

[2] V. Rodriguez, "Automotive component EMC testing: CISPR 25, ISO 11452–2 and equivalent standards," *IEEE Electromagnetic Compatibility Magazine,* vol. 1, pp. 83-90, 2012.

[3] C. F. M. Carobbi and D. Izzo, "Evaluation and Improvement of the Reproducibility of CISPR 25 ALSE Test Method," *IEEE Transactions on Electromagnetic Compatibility,* vol. 60, pp. 1069-1077, 2018.

[4] J. Jia, D. Rinas, and S. Frei, "Predicting the Radiated Emissions of Automotive Systems According to CISPR 25 Using Current Scan Methods," *IEEE Transactions on Electromagnetic Compatibility,* vol. 58, pp. 409-418, 2016.

[5] A. Radchenko, V. V. Khilkevich, N. Bondarenko, D. Pommerenke, M. Gonser, J. Hansen, *et al.*, "Transfer Function Method for Predicting the Emissions in a CISPR-25 Test-Setup," *IEEE Transactions on Electromagnetic Compatibility,* vol. 56, pp. 894-902, 2014.

[6] S. Shinde, K. Masuda, G. Shen, A. Patnaik, T. Makharashvili, D. Pommerenke, *et al.*, "Radiated EMI Estimation From DC-DC Converters With Attached Cables Based on Terminal Equivalent Circuit Modeling," *IEEE Transactions on Electromagnetic Compatibility,* pp. 1-8, 2018.

[7] H. Zhao, J. Yao, and S. Wang, "A Universal DM/CM Physical Model for Power Transformer EMI Analysis within both Conducted and Radiated Frequency Ranges," in *2018 IEEE Energy Conversion Congress and Exposition (ECCE)*, 2018, pp. 6592-6599.

[8] J. Yao, S. Wang, H. Zhao, Y. Zhang, Q. Wang, Y. Lu, *et al.*, "Measurement Techniques of CM Currents, Impedance and Voltages for Radiated EMI in Isolated Power Converters," in *2018 IEEE Symposium on Electromagnetic Compatibility, Signal Integrity and Power Integrity (EMC, SI & PI)*, 2018, pp. 438-443.

[9] J. Yao, Y. Li, H. Zhao, S. Wang, Q. Wang, Y. Lu, *et al.*, "Modeling and Reduction of Radiated Common Mode Current in Flyback Converters," in *2018 IEEE Energy Conversion Congress and Exposition (ECCE)*, 2018, pp. 6613-6620.

[10] Y. Li, H. Zhang, S. Wang, H. Sheng, C. P. Chng, and S. Lakshmikanthan, "Investigating Switching Transformers for Common Mode EMI Reduction to Remove Common Mode EMI Filters and Y-Capacitors in Flyback Converters," *IEEE Journal of Emerging and Selected Topics in Power Electronics,* vol. 6, pp. 2287-2301, 2018.

[11] J. Yao, M. El-Sharkh, Y. Li, S. Wang, and Z. Luo, "Investigation of Radiated EMI in Non-isolated Power Converters with Power Cables in Automotive Applications," in *2019 IEEE Energy Conversion Congress and Exposition (ECCE)*, 2019, pp. 6957-6964.

[12] H. Chen, T. Wang, L. Feng, and G. Chen, "Determining Far-Field EMI From Near-Field Coupling of a Power Converter," *IEEE Transactions on Power Electronics,* vol. 29, pp. 5257-5264, 2014.

[13] Y. Zhang, S. Wang, and Y. Chu, "Investigation of Radiated Electromagnetic Interference for an Isolated High-Frequency DC–DC Power Converter With Power Cables," *IEEE Transactions on Power Electronics,* vol. 34, pp. 9632-9643, 2019.